



Tandem achromatic metasurface for waveguide coupling in full-color AR displays

Downloaded from: <https://research.chalmers.se>, 2025-06-15 03:29 UTC

Citation for the original published paper (version of record):

Zhang, K., Fan, Z., Chen, K. et al (2025). Tandem achromatic metasurface for waveguide coupling in full-color AR displays. Optics Express, 33(2): 2019-2030. <http://dx.doi.org/10.1364/OE.549682>

N.B. When citing this work, cite the original published paper.



Tandem achromatic metasurface for waveguide coupling in full-color AR displays

KAIXIN ZHANG,^{1,2,†} ZHENGUI FAN,^{1,2,†} KANGKANG CHEN,^{1,2}
JIALE LIN,³ CHUNLEI HUANG,⁴ JUNYANG NIE,⁵ JIE SUN,^{1,2,6,8} 
QUN YAN,^{1,2,7} AND ENGUO CHEN^{1,2,9} 

¹National and Local United Engineering Laboratory of Flat Panel Display Technology, College of Physics and Information Engineering, Fuzhou University, Fuzhou, 350100, China

²Fujian Science & Technology Innovation Laboratory for Optoelectronic Information of China, Fuzhou, 350100, China

³State Key Laboratory of Internet of Things for Smart City, University of Macau, 519000, Macau, China

⁴College of Material and Chemical Engineering, Minjiang University, Fuzhou, 350108, China

⁵TCL China Star Optoelectronics Technology Co., Ltd, Shenzhen, 518132, China

⁶Quantum Device Physics Laboratory, Department of Microscience and Nanotechnology, Chalmers University of Technology, Göteborg, 41296, Sweden

⁷Rich Sense Electronics Technology Co., Ltd., Quanzhou, 362200, China

⁸jie.sun@fzu.edu.cn

⁹ceg@fzu.edu.cn

[†]These authors contributed equally to this work

Abstract: Waveguide coupling design is one of the most challenging topics in augmented reality (AR) near-eye displays (NED). The primary challenge stems from the necessity to simultaneously address two competing factors: the overall volume of the AR system and the occurrence of chromatic aberration. To address this issue, what we believe to be a novel tandem trilayer achromatic metasurface is specifically designed for waveguide coupling in AR NEDs, capable of achieving an achromatic effect in a nanometer-thin layer. By analyzing the influence of unit structure parameters on the phase delay of input electromagnetic waves, the optimal parameters are determined and the tandem trilayer achromatic metasurface structure is established. Simulation results show that the incident light can be deflected by 45°, 46°, and 45° at wavelengths of 440 nm ~ 470 nm, 520 nm ~ 550 nm, and 620 nm ~ 660 nm, respectively. The angular deviation error of the three primary colors is maintained lower than 1° in the AR waveguide, ensuring a satisfactory achromatic effect. This design provides a new solution for developing ultra-thin and compact optical systems for full-color AR NEDs.

© 2025 Optica Publishing Group under the terms of the [Optica Open Access Publishing Agreement](#)

1. Introduction

With the advancement of technology, head-mounted displays have become increasingly lightweight and compact, evolving into near-eye display (NED) systems in the form of glasses or protective eyewear. Among these, augmented reality (AR) stands out and has been widely employed in multimedia, intelligent interaction, sensing, and other various applications [1,2]. AR superimposes computer-generated virtual objects, scenes, or system prompts onto the real environment [3–5]. This integration allows for immersive experiences and interactive capabilities that can significantly enhance the perception of the real scene and enrich user engagement and functionality. As early as the 1950s, AR began to find applications in defense, and over the decades, it has evolved into an indispensable hardware carrier and medium for “metaverse” [6–9]. AR NED combined with micro-LED microdisplays will be the trend and focus of future research [10,11].

In recent years, the demand for AR displays has been continuously increasing, particularly for high-resolution, high-brightness micro-display devices with small volume and lightweight near-eye optical systems [12–14]. The optical engine module plays a crucial role in AR near-eye display devices, directly influencing imaging quality and manufacturing costs. Currently, AR near-eye display technology often blends and displays real scenes with virtual images through the design of various optical combiners. Traditional near-eye displays face technical challenges in balancing the field of view and volume. Subwavelength optical metasurfaces offer a promising solution for light modulation in AR optical engines, enabling enhanced performance and miniaturization. These metasurfaces, composed of subwavelength periodic structures arranged in a two-dimensional plane, provide unique properties that traditional materials cannot achieve. By manipulating the phase of light waves in a discontinuous manner, arbitrary control over anomalous reflection, anomalous refraction, and polarization of the optical field can be achieved, which have broadened the application scope of metasurfaces in AR near-eye optical systems [15–18].

Chromatic aberration correction is a crucial indicator in NED applications [19,20]. This optical aberration, stemming from the differential refraction of light based on its wavelength, poses a significant challenge in maintaining image quality and system performance [21]. Failure to address chromatic aberration can lead to detrimental effects on image sharpness, color accuracy, and overall system performance within NED applications. The adverse effects of chromatic aberration can be mitigated by utilizing specialized lens materials, designing precision optical coatings, or leveraging innovative technologies like metasurfaces [22,23]. These tailored approaches enable the precise manipulation of light to converge wavelengths at a common focal point, thereby enhancing image quality and system performance in NED applications. In 2018, G. Y. Lee et al. utilized components like dichroic mirrors to change the imaging positions of different wavelengths for chromatic aberration correction [24]. They employed a metasurface with a diameter of 20 mm and a numerical aperture of 0.61 to construct a prototype AR system, achieving a monochromatic field of view of 90° and a full-color imaging field of view (FOV) of 76°, with a co-polarized transmission efficiency reaching 79% in the red, green, and blue spectra. In 2021, T. Afra et al. designed a monocular optical waveguide display, using a crystalline silicon elliptical metasurface array as a coupler on a right trapezoidal waveguide [25]. This achieved an 80° horizontal large FOV, approximately 80% higher than the FOV in traditional waveguide systems based on diffractive gratings. In 2022, H. Boo et al. achieved a resolution of 1080 PPI and a FOV exceeding 40° through careful design of each unit in the metasurface [26]. The total input-output efficiency surpassed 1%. Simultaneously, utilizing a single metasurface waveguide for AR waveguides aids in controlling scalability and process yield [27].

The use of metasurfaces [28–32] for optical phase modulation can be summarized into three main methods: resonant phase modulation [33,34], transmission phase modulation [35,36], and geometric phase modulation [37,38]. Resonant phase modulation achieves abrupt phase changes by altering the resonant frequency, which is controlled by the geometric shape of nano-scale structures. Transmission phase modulation exploits the optical path difference generated as electromagnetic waves propagate, allowing for phase control. Geometric phase modulation involves adjusting the rotation angle of micro/nanostructures with identical dimensions to induce phase changes in light waves. Among these, metasurfaces designed based on the transmission phase principle typically consist of isotropic micro/nanostructures with highly symmetric characteristics [39,40]. Such metasurfaces exhibit insensitivity to the polarization of incident light, meaning that the phase response of nanostructures is independent of the polarization type of the incident light. Additionally, these structures are easy to achieve high efficiency [41], making them well-suited for optical waveguide-type AR optical engines. But a single-layer metasurface is hard to achieve achromatic effect.

Based on this, our paper proposes an effective design of a tandem multilayer metasurface aiming to achieve synchronized angular deflection for broadband spectrum. The designed

metasurface achieves transmission phase modulation by introducing an optical path difference generated during transmission of electromagnetic waves. This method allows for narrowband wavelength control, adjusting a small segment of the wavelength per layer, making it possible to independently correct three-primary-color chromatic aberration in tandem metasurface layers.

2. Principle

Mie scattering resonance provides a way to achieve high transmittance and full phase coverage, but its narrow bandwidth is limited by the resonance mode characteristics. It is based on the interaction between light waves and nanostructures in the medium, and its resonance characteristics are closely related to the geometric parameters of the nanostructures. By adjusting the dimensions of the nanostructure units, different electromagnetic responses can be achieved, allowing for phase adjustments and more [42,43].

A tandem multi-layer metasurface structure is designed for chromatic aberration correction that can deflect multiple wavelengths at the same angle. Through closely stacking metasurfaces of dielectric materials, independent control of multiple wavelengths is achieved, enhancing the efficiency of multiple wavelengths. A method for designing a multi-wavelength deflection metasurface structure with non-interacting layers is proposed. This involves achieving independent phase modulation at multiple wavelengths through closely stacked metasurfaces, with each layer controlling a different wavelength, providing the required phase for each specific wavelength. Each wavelength can be independently controlled without interference, ensuring that the deflection angles of emitted light for RGB are the same.

The tandem trilayer achromatic metasurface based AR waveguide component is shown in Fig. 1(a). The metasurface is based on cylindrical nanostructures with high aspect ratio. This circular shape of dielectric nanostructures has high efficiency and low sensitivity to incident angles, making it an ideal shape for transmission-phase metasurfaces. Here, the target wavelengths for the trilayer deflection metasurface are 465 nm, 530 nm, and 635 nm, respectively.

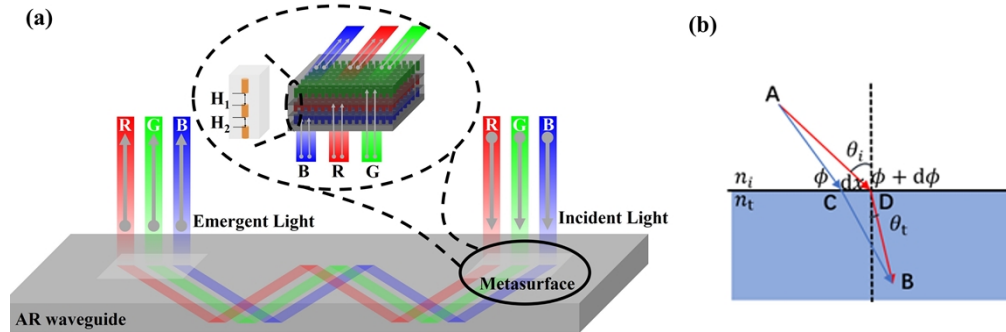


Fig. 1. Schematic diagram of (a) the AR waveguide component employing the tandem achromatic metasurface and (b) generalized Snell's law.

In Fig. 1(b), light is incident from point A in medium 1 to point B in medium 2, where the refractive index of medium 1 is n_i , the refractive index of medium 2 is n_t , the incidence angle is θ_i , and the refraction angle is θ_t . Suppose that there are two infinitely close optical paths propagating from point A to point B, namely ADB and ACB, represented by red and blue lines. The optical path ACB passes through the metasurface to produce a phase mutation of Φ , and the optical path ADB passes through the metasurface to produce a phase mutation of $\Phi + d\Phi$. Then, according to Fermat's theorem, the following equation can be obtained:

$$\Phi + d\Phi + k_0 n_t dx \cdot \sin \theta_t = \Phi + k_0 n_i dx \cdot \sin \theta_i \quad (1)$$

where, $k_0 = 2\pi/\lambda_0$, k_0 is the electromagnetic wave vector in vacuum, λ_0 is the wave velocity in vacuum, dx is the intersection distance of two optical paths through the metasurface. This derives the generalized Snell's law:

$$n_t \sin \theta_t - n_i \sin \theta_i = \frac{\lambda_0}{2\pi} \cdot \frac{d\Phi}{dx} \quad (2)$$

where n_t is the refractive index of the background material for the transmission wave, θ_t represents the angle of the transmission wave, and n_i is the refractive index of the background material for the incident wave, θ_i represents the angle of the incident wave, λ_0 denotes the wavelength of the incident light, while $d\Phi$ represents the phase difference. Additionally, dx is defined as the period of a single cylinder.

3. Simulation

3.1. Parameter optimization

All-dielectric phase gradient metasurface is designed by the above method. The unit structure is shown in Fig. 2(a). The decision to utilize cylindrical shapes rather than other geometries in the design of metasurface units stems from the central symmetry inherent in cylindrical metasurface units. This symmetry imparts unique polarizing insensitivity properties to metasurface devices composed of such nanocrystal arrays. The cell structure period (P), nanometer column height (H), and nanometer column radius (R) are the three basic parameters that control the amplitude and phase of the all-dielectric metasurface transmission. The following part will emphasize on the analysis and selection of chromatic aberration-corrected metasurface unit structure parameters.

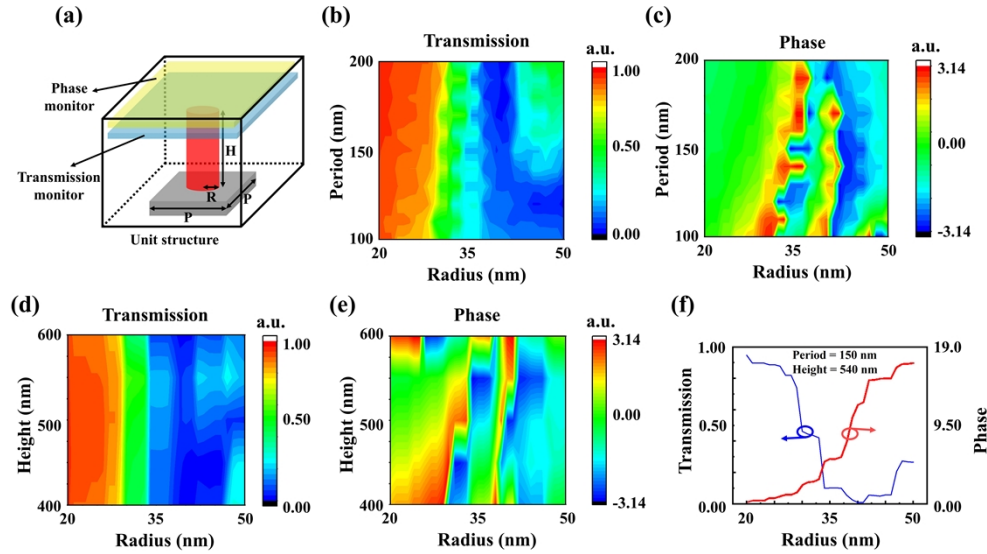


Fig. 2. (a) Simulation diagram of metasurface unit structure. (b)-(e) Transmittance and phase delay changes with radius and period or height, respectively. (f) The curve of transmittance and phase delay with radius (Period = 150 nm and Height = 540 nm).

Firstly, the unit structure parameters were scanned at a wavelength of 465 nm. The real part of the refractive index of Si at 465 nm is 4.53171, with an imaginary part of 0.13306. An initial sampling was performed over a large range to determine an appropriate parameter range. Based on the preliminary scan data, the unit period that satisfies a 2π phase delay is roughly between 100 nm and 200 nm.

Figure 2(b) and 2(c) illustrates the variation of the transmittance and the phase delay with unit period and nanostructure's radius, respectively. The selection of the period requires that the average transmittance of the nanostructures with different radii in this period should be as high as possible. Moreover, the phase delay of the nanostructures should be as smooth as possible. Considering the changes in transmittance and phase delay, a unit period size of 150 nm was selected.

Next is the definition of the unit structure's height. Considering manufacturing feasibility, the aspect ratio of the unit structure should not be too large, and when the aspect ratio of the unit structure is too small, it cannot guarantee that the control of the wave front of the unit structure covers the phase delay of 2π . At the same time, the radius range and period of the unit structure are 20 nm ~ 50 nm and 150 nm, respectively. Figure 2(d) demonstrates that the transmittance gradually decreases with the increase in the height and radius of the unit structure, while Fig. 2(e) shows that the phase delay increases gradually with the increase in the height and radius, ranging from -3.14 rad to 3.14 rad. Thus, it is possible to achieve phase control greater than 2π with the height scanning. As with the period, the unit period size was chosen to be 540 nm, considering the changes in transmittance and phase delay.

Combining with the highest average transmittance, the unit period is set at 150 nm, the height is 540 nm, and the radius is 20 nm ~ 50 nm. The refractive indices of Si and SiO₂ were taken from a FDTD related material database. At this time, the change curve of the transmittance and phase delay of the unit structure with the radius is shown in Fig. 2(f). According to the above method, the similar simulation is performed for green light and red light at 530 nm and 635 nm, and the corresponding data is obtained. See Supplement 1 for details.

The dielectric nanoscale cylinder of the metasurfaces have high efficiency and low sensitivity to incident angles, making them ideal shapes for transmission phase metasurfaces. To validate the principles, a trilayer deflection metasurface was designed for target wavelengths of 465 nm, 530 nm, and 635 nm. The heights of the cylindrical structure for the upper, middle, and lower layers were 530 nm, 635 nm, and 465 nm, respectively, with a substrate material of SiO₂ and a refractive index around 1.51 in the visible light range. For the upper green metasurface, $\lambda_1 = 530$ nm, $dx_1 = 170$ nm, and $d\Phi_1 = 2\pi/3$; For the middle red metasurface, $\lambda_2 = 635$ nm, $dx_2 = 200$ nm, and $d\Phi_2 = 2\pi/3$; For the lower blue metasurface, $\lambda_3 = 465$ nm, $dx_3 = 150$ nm, and $d\Phi_3 = 2\pi/3$. According to Eq. (1), the calculated deflection angles are $\theta_{i1} = 45.23^\circ$ for green light after passing through the upper metasurface, $\theta_{i2} = 46.86^\circ$ for red light after passing through the middle metasurface, and $\theta_{i3} = 45.45^\circ$ for blue light after passing through the lower metasurface, respectively. The specific radii and corresponding phases are listed in Table 1. It is intentional to set $d\Phi = 2\pi/3$ instead of $\pi/3$ or π . Choosing $\pi/3$ does not enable the incident light to achieve the full reflection condition within the waveguide thereby diminishing its effectiveness. Furthermore, opting for π would result in a poor deflection effect due to the extensive phase span, thereby compromising the metasurface's performance. All the deflection angles are greater than the total internal reflection angle in the waveguide.

Table 1. Mapping results between phase delay and metasurface radius.

	Metasurface1			Metasurface2			Metasurface3		
Phase	$2\pi/3$	$4\pi/3$	2π	$2\pi/3$	$4\pi/3$	2π	$2\pi/3$	$4\pi/3$	2π
Diameter (nm)	60	68	76	100	116	126	84	94	104

3.2. Model establishment

Single-layer metasurface was designed and simulated with its corresponding wavelength. Due to the narrow response bandwidth of the transmission phase metasurface, a metasurface structure designed for the wavelength of 465 nm may cause beam deflection when the 465 nm light passes

through it, while the 530 nm and 635 nm light pass directly through without any response. Similarly, when metasurface structures are designed for the other two wavelengths, there is no response when other wavelengths pass through.

Figure 3(a)-(c) shows the far-field energy distribution of light at 465 nm, 530 nm, and 635 nm after passing through the three separate single-layer metasurfaces, respectively. It is obvious that the energy is mainly distributed in 45° , 46° and 45° respectively, which is consistent with the calculated results of Eq. (1) and meets the expected requirements. Figure 3(d)-(f) are the vertical cross section intensity under the cartesian coordinates, which are consistent with the light field distribution. Figure 3(g)-(i) verifies the angular deflection of single layer metasurface at different wavelengths. Figure 3(g) illustrates the metasurface layer responsible for deflecting 465 nm wavelength light, demonstrating that deflection occurs only when the light with this wavelength is incident. Figure 3(h) depicts the metasurface layer that deflects 530 nm wavelength light, allowing the 465 nm and 635 nm beams to pass directly through. Figure 3(i) presents the metasurface layer controlling the deflection of 635 nm wavelength light, with the 465 nm and 530 nm beams passing directly through the metasurface.

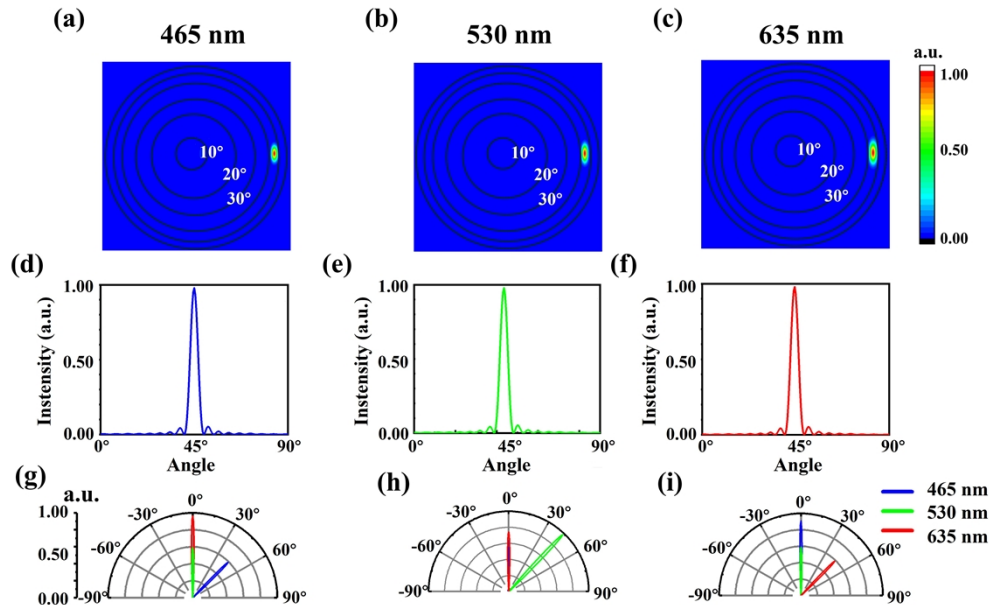


Fig. 3. (a)-(c) The normalized far-field distribution of energy. The intensity distribution of vertical cross sections under (d)-(f) cartesian and (g)-(i) polar coordinates.

A tandem multilayer structure can be established after combining the three metasurfaces. If the spacing between each layer is inappropriate, coupling effects may occur. Coupling effects can lead to the failure of phase modulation of the unit structure, meaning that the incident beam on the metasurface structure will not undergo deflection, thus failing to achieve the purpose of controlling the beam.

Figure 4(a) shows a schematic diagram of the tandem unit structure. The value of the spacing $H1$ is set to 0, 50 nm, 100 nm, 150 nm, and 200 nm, respectively. When $H1$ changes, $H2$ also changes accordingly, and an optimal result is solved. During the simulation, all energy distributions of the incident light are confined within $\pm 5^\circ$. Consequently, we define light within the calculated deflection angle of $\pm 5^\circ$ as effectively deflected light, and light at other angles as stray light. The design effectiveness was evaluated by calculating the proportion of stray light relative to the total light, with a lower proportion indicating a superior effect. Specific data, which

are shown in Table 2, demonstrate that the metasurface yields optimal results with configurations of $H_1 = 50$ nm and $H_2 = 150$ nm. Regarding practical material choices, silicon (Si) is selected for the metasurface material because it has a high refractive index in the visible light spectrum. This property enables the metasurface units to achieve 2π phase coverage with a smaller period, allowing for a greater number of units to be placed within the same area, thereby facilitating finer phase control. Additionally, PMMA is considered as one of the potential alternatives of transparent materials, because it not only has a simple fabrication process but also offers high transparency. As for fabrication techniques, the metasurface we designed is envisioned to be created by initially fabricating a single-layer metasurface, followed by a stacking method to realize the tandem achromatic metasurface. The techniques required for this process involve initially using Chemical Vapor Deposition to uniformly grow the metasurface material [44,45], followed by employing electron-beam lithography to pattern the metasurface structures [46–48], and concluding with the deposition of a spin-coated PMMA layer with a fixed thickness to encapsulate the structures. This process would be repeated three times to achieve the tandem achromatic metasurface. Regarding tolerances, precise control of the spacing can be achieved by adjusting the PMMA solution concentration and the rotational speed [49].

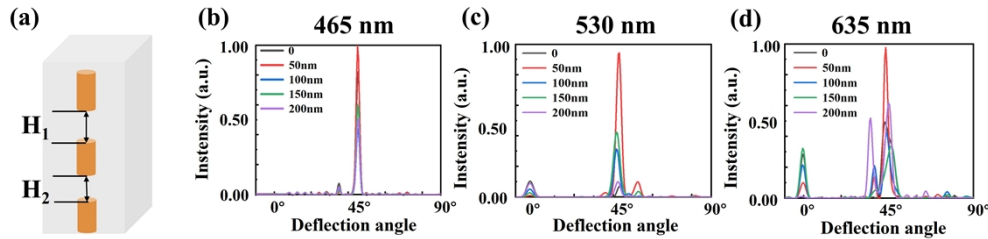


Fig. 4. (a) Schematic diagram of the tandem unit of the trilayer metasurface. (b)-(d) Deflection angles varying with spacing at different wavelengths.

Table 2. The proportion of stray light in the emergent light under different conditions.

	$H_1 = 0$ nm $H_2 = 200$ nm	$H_1 = 50$ nm $H_2 = 150$ nm	$H_1 = 100$ nm $H_2 = 100$ nm	$H_1 = 150$ nm $H_2 = 50$ nm	$H_1 = 200$ nm $H_2 = 0$ nm
$\lambda = 465$ nm	21.02%	23.30%	23.95%	20.75%	18.42%
$\lambda = 530$ nm	12.69%	9.28%	14.52%	27.02%	65.07%
$\lambda = 635$ nm	13.64%	14.65%	25.00%	50.05%	85.41%
Average proportion	15.78%	15.74%	21.16%	32.61%	56.30%

The relationship between the deflection angle and the spacing between metasurfaces is shown in Fig. 4(b)-(d). Figure 4(b) indicates that the spacing has no effect on the deflection angle at the wavelength of 465 nm. Figure 4(c) shows that the spacing has a certain effect on its transmittance, with the highest transmittance when $H_1 = 50$ nm and $H_2 = 150$ nm at the wavelength of 530 nm. Figure 4(d) shows the spacing also has a certain effect on its transmittance at the wavelength of 635 nm. From the simulation results of 530 nm and 635 nm, it can be seen that coupling effects between unit structures will affect phase modulation. The deflection angle and transmittance of the three wavelengths are optimal when $H_1 = 50$ nm and $H_2 = 150$ nm.

4. Results and discussion

4.1. Full-color achromatic effect

Figure 5(a) shows the schematic diagram of the tandem trilayer metasurface. Plane waves with wavelengths of 465 nm, 530 nm, and 635 nm were used as incident light sources. Due to the

coupling effects between layers, wavelength phase modulation may be affected, resulting in stray light at other angles. Figure 5(b) shows a cartesian diagram of the vertical cross-sectional intensity of the three wavelengths. Their deflection angles almost overlap, indicating that the trilayer metasurface is very effective for chromatic aberration correction. Figure 5(c)-(e) depicts the far-field energy distribution passing through the tandem trilayer metasurface structure when the incident light wavelength is 465 nm, 530 nm, and 635 nm, respectively. In Fig. 5(c), there exists certain stray light near 20° , which does not reach the total internal reflection angle. In Fig. 5(d), there is almost no stray light, and the coupling effect is minimal. In Fig. 5(e), the light field is mostly distributed at the designed angle, with some zero-order diffraction at 0° , which, however, will directly emit in the optical waveguide, thus not introducing stray light. The above results have demonstrated the achromatic effect of the tandem trilayer metasurface on incident light of different wavelengths, showing great application potential in full-color AR NEDs.

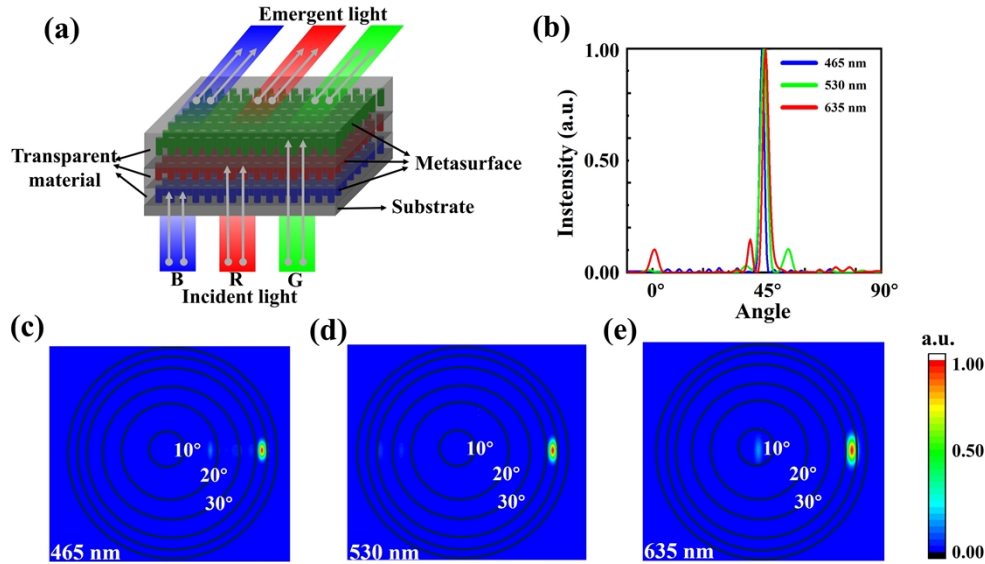


Fig. 5. (a) Schematic diagram for the tandem trilayer achromatic metasurface. (b) Vertical cross-sectional intensity distribution map. (c)-(e) Far-field energy distribution diagram.

In addition, we have taken an in-depth look at the underlying physical mechanisms of the tandem trilayer metasurface, aiming to gain a more complete understanding of the proposed structure. Figure 6 reveals the internal mechanism of the tandem trilayer metasurface to achieve achromatic aberration. Figure 6(a)-(c) shows the electric field intensity distribution of the blue metasurface when the incident light of 465 nm, 530 nm and 635 nm passes through it, respectively. As shown in Fig. 6(a), when 465 nm light passes through the blue metasurface, a strong Mie resonance effect is formed between the blue light and the unit structure. The intensity of the electric field changes significantly, thus enabling the blue metasurface to deflect the light of 465 nm wavelength. As the wavelength increases, as shown in Fig. 6(b), when the 530 nm light passes through the blue metasurface layer, only the electric field distribution around the cylinder can be observed, indicating that the Mie resonance is almost suppressed, allowing the green light to pass through almost without impact. Figure 6(c) shows that when the wavelength increases to 635 nm, the cylindrical structure has little influence on the red light, which enables the red light to directly pass through the blue metasurface.

Figure 6(d)-(f) shows the electric field intensity distribution of the green metasurface deflection layer when the incident light of 465 nm, 530 nm and 635 nm passes through it, respectively. As shown in Fig. 6(d), when 465 nm light passes through the green metasurface, the electric

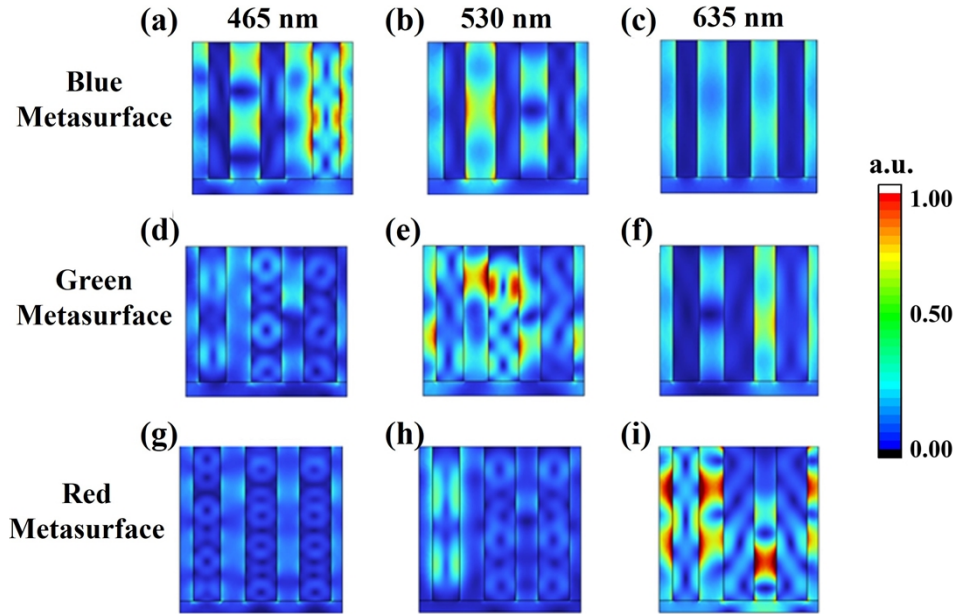


Fig. 6. Electric field intensity distribution at different wavelengths in different deflection layers of the tandem achromatic metasurface.

field strength is weak, which indicates that the Mie resonance is not well excited, resulting in minimal blue light deflection. When the wavelength of incident light is increased to 530 nm, as shown in Fig. 6(e), strong electric field distribution appears inside and outside the cylindrical structure, thus achieving effective Mie resonance excitation, which enables green light to achieve deflection effect at the required angle. When the wavelength of incident light further increases to 635 nm, the electric field is only distributed outside the cylindrical structure, which enables the red light to pass through the metasurface, as shown in Fig. 6(f). Figure 6(g)-(i) shows the similar phenomenon for red metasurface layer.

Overall, the above results indicate that the tandem trilayer metasurface can achieve efficient excitation of resonant modes at the corresponding wavelengths while almost avoiding influences on other wavelengths.

4.2. Broadband achromatic effect

The wavelength bandwidth response of the tandem metasurface was evaluated via broadband simulations. In practical applications, the wavelength of the light source is not limited to a single wavelength but spans a range of wavelengths. Here, the simulation range for blue light wavelengths was from 440 nm to 470 nm, for green light wavelengths 520 nm to 550 nm, and for red light wavelengths 620 nm to 660 nm. It can be observed from Fig. 7(a) that different blue light with 440 nm ~ 470 nm exhibit almost identical deviation angles while incident normally. This consistency is attributed to the bottom blue metasurface. Figures 7(b) and 7(c) depict the simulation results for green and red light, respectively. For different wavelengths passing through the metasurface, there are slight angular deviations within an acceptable range. This variation stems from differences in the structure's response to different wavelengths.

The incident angle is also a key factor in evaluating the metasurface's performance. The deviation angle of incident light is set at 5° for wavelengths of 465 nm, 530 nm, and 635 nm for simulation. As shown in Fig. 7(d)-(f), when the wavelength is 465 nm and the incident angle is 5° , the deviation angle is 47.9° , with slight scattered light at other angles. For a wavelength of

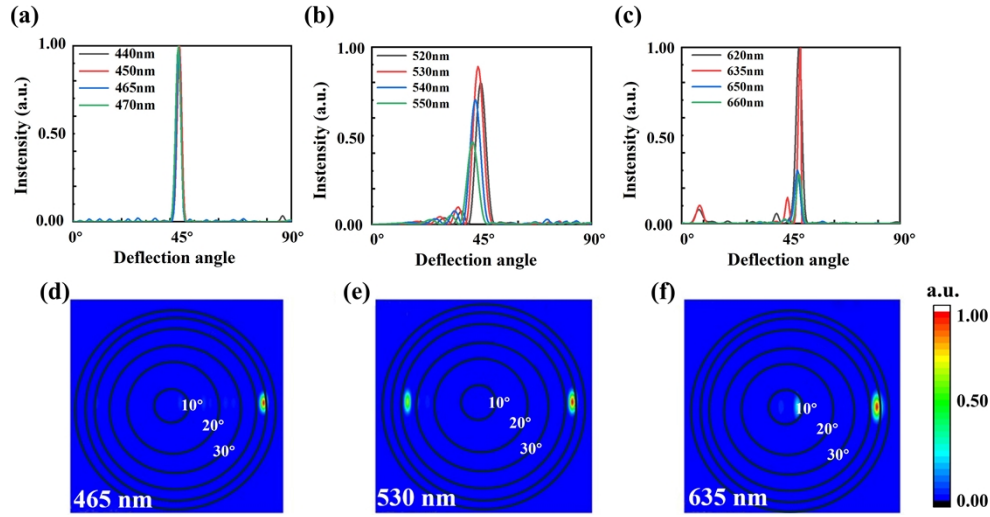


Fig. 7. (a)-(c) The vertical cross-sectional intensity distribution and (d)-(f) far-field energy distribution of the tandem achromatic metasurface under different wavebands or incident angle, respectively.

530 nm and an incident angle of 5° , the deviation angle is 48.2° . The light field plot for 530 nm indicates certain energy spots around -40° , which is caused by additional resonances occurring due to oblique incidence, resulting in phase modulation deviation and tilting of the wavefront towards other angles. For a wavelength of 635 nm and an incident angle of 5° , the deviation angle is 49.4° , with another light spot near 10° for similar reasons as with 530 nm. However, this angle does not cause chromatic aberration as it does not undergo total internal reflection within the waveguide. Therefore, when designing the achromatic metasurface for waveguide coupling, it is essential to consider the impact of the incident angle on performance. Further optimization of the structure may be required to accommodate larger incident angle effectively. When the deviation of the incidence angle is greater than 5° or greater, not only is the deflection angle significantly reduced, failing to meet the waveguide's requirement for total reflection, but the proportion of stray light will also increase substantially. A preliminary strategy is to pass the incident light through a prepositive focal lens before it enters the tandem achromatic metasurface. This would keep the divergence angle within the range that the tandem achromatic metasurface can efficiently deflect. In summary, exploring the efficacy of metasurfaces under larger angular deviations in incident light represents a significant avenue for our future research efforts.

5. Conclusions

The paper presents a novel tandem trilayer achromatic metasurface for waveguide coupling of NEDs. First, the metasurface structures for 465 nm, 530 nm, and 635 nm were designed respectively, ensuring that the metasurface structures for each wavelength had limited effect on the other two wavelengths. Then, the three structures were stacked, and the optimal layer spacing was obtained through scanning and simulation. The corresponding simulation analysis was carried out in the case of wide wavelength incidence. Results show that this design successfully achieves a deflection of 45° at a wavelength of 440 nm ~ 470 nm, a deflection of 46° at a wavelength of 520 nm ~ 550 nm, and a deflection of 45° at a wavelength of 620 nm ~ 660 nm. The angular deflection error of the three primary colors is maintained lower than 1° , which provides a good achromatic effect for NEDs. Moreover, the large angle incidence is analyzed, which provides technical support for the subsequent realization of the waveguide coupling. This innovative

design showcases considerable potential for achromatic AR NEDs, thereby markedly enhancing the performance and reliability of optical components within NED applications.

Funding. National Key Research and Development Program of China (2022YFB3603503); National Natural Science Foundation of China (62175032, 62005111, 62404046); Key Science and Technology Project Program of Fujian Province (2024HZ022005); Science Fund for Distinguished Young Scholars of Fujian Province (2024J010046); Natural Science Foundation of Fujian Province (2022J011124); Fujian Science and Technology Innovation Laboratory for Optoelectronic Information of China (2024CXY106, 2021ZZ122).

Disclosures. The authors declare no conflicts of interest.

Data availability. Data underlying the results presented in this paper are not publicly available at this time but may be obtained from the authors upon reasonable request.

Supplemental document. See [Supplement 1](#) for supporting content.

Reference

1. T. Zhan, K. Yin, J. H. Xiong, *et al.*, "Augmented Reality and Virtual Reality Displays: Perspectives and Challenges," *iScience* **23**(8), 101397 (2020).
2. C. Chang, K. Bang, G. Wetzstein, *et al.*, "Toward the next-generation VR/AR optics: a review of holographic near-eye displays from a human-centric perspective," *Optica* **7**(11), 1563–1578 (2020).
3. J. H. Xiong, E. L. Hsiang, Z. Q. He, *et al.*, "Augmented reality and virtual reality displays: emerging technologies and future perspectives," *Light: Sci. Appl.* **10**(1), 216 (2021).
4. H. J. Jang, J. Y. Lee, G. W. Baek, *et al.*, "Progress in the development of the display performance of AR, VR, QLED and OLED devices in recent years," *J. Inf. Disp.* **23**(1), 1–17 (2022).
5. K. Yin, E. L. Hsiang, J. Y. Zou, *et al.*, "Advanced liquid crystal devices for augmented reality and virtual reality displays: principles and applications," *Light: Sci. Appl.* **11**(1), 22 (2022).
6. H. Wang, H. S. Ning, Y. J. Lin, *et al.*, "A Survey on the Metaverse: The State-of-the-Art, Technologies, Applications, and Challenges," *IEEE Internet Things J.* **10**(16), 14671–14688 (2023).
7. W. Y. B. Lim, Z. H. Xiong, D. Niyato, *et al.*, "Realizing the Metaverse with Edge Intelligence: A Match Made in Heaven," *IEEE Wirel. Commun.* **30**(4), 64–71 (2023).
8. P. A. Kara, R. R. Tamboli, V. K. Adhikarla, *et al.*, "Connected without disconnection: Overview of light field metaverse applications and their quality of experience," *Displays* **78**, 102430 (2023).
9. Y. Li, H. A. Jiang, Y. G. Yan, *et al.*, "Highly efficient and ultra-compact micro-LED pico-projector based on a microlens array," *J. Soc. Inf. Disp.* **31**(7), 483–493 (2023).
10. L. W. Deng, X. Zhang, Y. G. Yan, *et al.*, "Ambient contrast ratio of quantum-dot color-converted micro-LED displays," *Results Phys* **48**, 7 (2023).
11. Y. Z. Liu, T. W. Xia, A. C. Du, *et al.*, "Omnidirectional color shift suppression of full-color micro-LED displays with enhanced light extraction efficiency," *Opt. Lett.* **48**(7), 1650–1653 (2023).
12. X. Zhang, A. Chen, T. Yang, *et al.*, "Tripling Light Conversion Efficiency of μ LED Displays by Light Recycling Black Matrix," *IEEE Photonics J.* **15**(3), 1–7 (2022).
13. X. P. Hu, J. H. Cai, Y. Z. Liu, *et al.*, "Design of inclined omni-directional reflector for sidewall-emission-free micro-scale light-emitting diodes," *Opt. Laser Technol.* **154**, 9 (2022).
14. E. G. Chen, Z. M. Yao, Z. G. Fan, *et al.*, "Collimated LED Array With Mushroom-Cap Encapsulation for Near-Eye Display Projection Engine," *IEEE J. Sel. Top. Quantum Electron.* **30**(2), 10 (2024).
15. N. F. Yu, P. Genevet, M. A. Kats, *et al.*, "Light Propagation with Phase Discontinuities: Generalized Laws of Reflection and Refraction," *Science* **334**(6054), 333–337 (2011).
16. M. Khorasaninejad, W. T. Chen, R. C. Devlin, *et al.*, "Metalenses at visible wavelengths: Diffraction-limited focusing and subwavelength resolution imaging," *Science* **352**(6290), 1190–1194 (2016).
17. N. F. Yu and F. Capasso, "Flat optics with designer metasurfaces," *Nat. Mater.* **13**(2), 139–150 (2014).
18. A. Zhan, S. Colburn, C. M. Dodson, *et al.*, "Metasurface Freeform Nanophotonics," *Sci. Rep.* **7**(1), 9 (2017).
19. T. Zhan, J. Y. Zou, J. H. Xiong, *et al.*, "Practical chromatic aberration correction in virtual reality displays enabled by cost-effective ultra-broadband liquid crystal polymer lenses," *Adv. Opt. Mater.* **8**(2), 1901360 (2020).
20. Z. Q. Zhang, J. Liu, Q. K. Gao, *et al.*, "A full-color compact 3D see-through near-eye display system based on complex amplitude modulation," *Opt. Express* **27**(5), 7023–7035 (2019).
21. L. Waller, S. S. Kou, C. J. R. Sheppard, *et al.*, "Phase from chromatic aberrations," *Opt. Express* **18**(22), 22817–22825 (2010).
22. H. G. B. Gowda, M. C. Wapler, and U. Wallrabe, "Tunable doublets: piezoelectric glass membrane lenses with an achromatic and spherical aberration control," *Opt. Express* **30**(26), 46528–46540 (2022).
23. R. Sawant, D. Andr  n, R. J. Marins, *et al.*, "Aberration-corrected large-scale hybrid metalenses," *Optica* **8**(11), 1405–1411 (2021).
24. G. Y. Lee, J. Y. Hong, S. Hwang, *et al.*, "Metasurface eyepiece for augmented reality," *Nat. Commun.* **9**(1), 4562 (2018).
25. T. Afra, M. R. Salehi, and E. Abiri, "Design of two compact waveguide display systems utilizing metasurface gratings as couplers," *Appl. Opt.* **60**(28), 8756–8765 (2021).

26. H. Boo, Y. S. Lee, H. B. Yang, *et al.*, “Metasurface wavefront control for high-performance user-natural augmented reality waveguide glasses,” *Sci. Rep.* **12**(1), 12 (2022).
27. D. K. Nikolov, A. Bauer, F. Cheng, *et al.*, “Metaform optics: Bridging nanophotonics and freeform optics,” *Sci. Adv.* **7**(18), eabe5112 (2021).
28. J. B. Wu, Z. Shen, S. J. Ge, *et al.*, “Liquid crystal programmable metasurface for terahertz beam steering,” *Appl. Phys. Lett.* **116**(13), 5 (2020).
29. H. S. Ee and R. Agarwal, “Tunable Metasurface and Flat Optical Zoom Lens on a Stretchable Substrate,” *Nano Lett.* **16**(4), 2818–2823 (2016).
30. A. Zhan, S. Colburn, R. Trivedi, *et al.*, “Low Contrast Dielectric Metasurface Optics,” *Conference on Lasers and Electro-Optics*. (2016).
31. Q. Ma, G. D. Bai, H. B. Jing, *et al.*, “Smart metasurface with self-adaptively reprogrammable functions,” *Light: Sci. Appl.* **8**(1), 12 (2019).
32. S. J. Li, B. W. Han, Z. Y. Li, *et al.*, “Transmissive coding metasurface with dual-circularly polarized multi-beam,” *Opt. Express* **30**(15), 26362–26376 (2022).
33. N. Dabidian, I. Kholmanov, A. B. Khanikaev, *et al.*, “Electrical Switching of Infrared Light Using Graphene Integration with Plasmonic Fano Resonant Metasurfaces,” *ACS Photonics* **2**(2), 216–227 (2015).
34. Z. X. Shen, S. H. Zhou, X. A. Li, *et al.*, “Liquid crystal integrated metalens with tunable chromatic aberration,” *Adv. Photonics* **2**(03), 7 (2020).
35. J. Hu, S. Bandyopadhyay, Y. H. Liu, *et al.*, “A Review on Metasurface: From Principle to Smart Metadevices,” *Front. Phys.* **8**, 586087 (2021).
36. Z. H. Liu, W. B. Feng, Y. Long, *et al.*, “A Metasurface Beam Combiner Based on the Control of Angular Response,” *Photonics* **8**(11), 12 (2021).
37. W. T. Chen, A. Y. Zhu, V. Sanjeev, *et al.*, “A broadband achromatic metalens for focusing and imaging in the visible,” *Nat. Nanotechnol.* **13**(3), 220–226 (2018).
38. E. Maguid, I. Yulevich, M. Yannai, *et al.*, “Multifunctional interleaved geometric-phase dielectric metasurfaces,” *Light: Sci. Appl.* **6**(8), e17027 (2017).
39. J. P. Huang, Z. L. Hu, X. Gao, *et al.*, “Unidirectional-emitting GaN-based micro-LED for 3D display,” *Opt. Lett.* **46**(14), 3476–3479 (2021).
40. E. Khaidarov, Z. T. Liu, R. Paniagua-Dominguez, *et al.*, “Control of LED Emission with Functional Dielectric Metasurfaces,” *Laser Photonics Rev.* **14**(1), 8 (2020).
41. E. G. Chen, M. Y. Zhao, K. K. Chen, *et al.*, “Metamaterials for light extraction and shaping of micro-scale light-emitting diodes: from the perspective of one-dimensional and two-dimensional photonic crystals,” *Opt. Express* **31**(11), 18210–18226 (2023).
42. K. X. Zhang, W. P. Wu, J. D. Shao, *et al.*, “Substrate-thickness dependence of negative-index metamaterials at optical frequencies,” *Appl. Phys. Lett.* **124**(10), 6 (2024).
43. E. Chen, Z. Fan, K. Zhang, *et al.*, “Broadband beam collimation metasurface for full-color micro-LED displays,” *Opt. Express* **32**(6), 10252–10264 (2024).
44. X. Zhou, L. Gan, W. Tian, *et al.*, “Ultrathin SnSe₂ flakes grown by chemical vapor deposition for high-performance photodetectors,” *Adv. Mater.* **27**(48), 8035–8041 (2015).
45. K. Xia, C. Wang, M. Jian, *et al.*, “CVD growth of fingerprint-like patterned 3D graphene film for an ultrasensitive pressure sensor,” *Nano Res.* **11**(2), 1124–1134 (2018).
46. H. H. Hsiao, C. H. Chu, and D. P. Tsai, “Fundamentals and applications of metasurfaces,” *Small Methods* **1**(4), 1600064 (2017).
47. Y. Chen, “Nanofabrication by electron beam lithography and its applications: A review,” *Microelectron. Eng.* **135**, 57–72 (2015).
48. D. Wang, K. D. Xu, S. Luo, *et al.*, “A high Q-factor dual-band terahertz metamaterial absorber and its sensing characteristics,” *Nanoscale* **15**(7), 3398–3407 (2023).
49. Y. Yan, Y. Zhuang, Y. Geng, *et al.*, “Effect of elastic modulus of PMMA films on its machinability by AFM-based nanoscratching method,” *Proc. SPIE* **9283**, 92830F (2014).